Overcoming chemical equilibrium limitations using a thermodynamically reversible chemical reactor

Ian S. Metcalfe[1*], Brian Ray[1], Catherine Dejoie[2], Wenting Hu[1], Chris de Leeuwe[1], Cristina Dueso[1], Francisco R. García-García[3], Cheuk-Man Mak[1], Evangelos I. Papaioannou[1], Claire. R. Thompson[1] and John. S. O. Evans[4]

[1]School of Engineering, Newcastle University, Newcastle-upon-Tyne NE1 7RU, U.K.

[2]European Synchrotron Radiation Facility, 71 avenue des Martyrs, 38043 Grenoble, France

[3]School of Engineering, The University of Edinburgh, Edinburgh EH9 3FB, U.K.

[4]Department of Chemistry, Durham University, Durham DH1 3LE, U.K.

All real processes be they chemical, mechanical or electrical, are thermodynamically irreversible and therefore suffer from thermodynamic losses. Here, we report the design and operation of a chemical reactor capable of approaching thermodynamically-reversible operation. The reactor was employed for hydrogen production via the water-gas shift reaction, an important route to 'green' hydrogen. The reactor avoids mixing reactant gases by transferring oxygen from the (oxidising) water stream to the (reducing) carbon monoxide stream via a solid-state oxygen reservoir consisting of a perovskite phase ($La_{0.6}Sr_{0.4}FeO_{3-\delta}$). This reservoir is able to remain close to equilibrium with the reacting gas streams because of its variable degree of non-stoichiometry and thus develops a 'chemical memory' which we employ to approach reversibility. We demonstrate this memory using operando, spatially-resolved, real-time, high-resolution x-ray powder diffraction on a working reactor. The design leads to a reactor unconstrained by overall chemical equilibrium limitations, which can produce essentially pure hydrogen and carbon dioxide as separate product streams.

Reducing thermodynamic losses within the chemical industry has driven the design of highly efficient heat and mass transfer devices as well as the methodologies to enable such design[1]. However, the heart of any chemical process, the chemical transformation occurring within the reactor, has not yet received the same level of attention; there is currently no recipe for producing a thermodynamically reversible chemical reactor and most reactors manifest very significant irreversibilities[2]. Here we design and operate such a thermodynamically reversible reactor. One impact of the reactor is its ability to overcome overall reaction equilibrium limitations. This property is significant as many chemical reactions are reversible in nature and their conversions are limited by reaction equilibrium. Such limitations leads to incomplete conversion of reactants, which then exit the reactor mixed with the products. This results in enormous cost to the chemical industry which must design and operate complex separation schemes to purify products. Although Dudukovic[3] identifies combining reaction and separation as a key means of avoiding such equilibrium constraints, there have, until now, been no ways of avoiding equilibrium constraints without the need for a simultaneous separation.

Chemical transformations are conventionally performed via 'mixed' reactions. Multiple reactants, initially separate, are mixed, the reaction mixture is heated to the reaction temperature and the reaction is allowed to proceed. The very act of mixing results in significant thermodynamic losses (one will inevitably need to expend energy to separate the reactants and the individual products). It is, however, possible to avoid mixing using a dynamic approach often referred to as chemical looping[4-7]. Indeed some of the potential thermodynamic advantages of such an approach have been recognised for e.g. combustion processes[8,9]. There has, however, been no recognition of how a dynamic or 'unmixed' approach could be used to overcome overall reaction equilibrium constraints.

Here we consider the reversible water-gas shift (WGS) reaction,

$H_2O + CO \rightleftarrows H_2 + CO_2$ Reaction 1

where H_2O is reacted with CO to produce H_2 and CO_2. Reaction 1 is key to many H_2 production processes and performed on a very large scale industrially (total capacity of 50 million tons per annum[10]). The reaction is equilibrium limited (Fig. 1a and Supplementary Video 1; a high-resolution version of the video can also be found at http://nuvision.ncl.ac.uk/Play/18143) and this leads to significant process complexity involving multiple reaction stages and separation. Overcoming this equilibrium limitation through the use of membranes[11-13] and CO_2 absorption[14-19] has attracted considerable attention in the past. In a chemical-looping WGS reactor, H_2O (high oxidising potential) is first passed over a solid phase carrier of oxygen (oxygen carrier material or OCM) that accepts oxygen resulting in the production of H_2. Then in a second step CO (low oxidising potential) is passed over the solid phase, removing oxygen to produce CO_2.

Step 1, H_2O-feed, bed-oxidation half cycle:

$H_2O + [OCM] \rightleftarrows H_2 + O[OCM]$ Reaction 2

Step 2, CO-feed, bed-reduction half cycle:

$CO + O[OCM] \rightleftarrows CO_2 + [OCM]$ Reaction 3

Thus we avoid gas-phase mixing of the H_2O and CO reactants and exploit the fact that the WGS reaction is an oxygen transfer reaction by performing the transfer in two separate steps

(a H_2O-feed, bed-oxidation half cycle and CO-feed, bed-reduction half cycle) through the use of an OCM. The conversion to products is then no longer limited by the chemical equilibrium of Reaction 1 but rather by the individual equilibria associated with Reactions 2 and 3. Conventional OCMs, such as metal-metal oxides, function by donating oxygen and receiving oxygen, at the fixed oxygen chemical potentials associated with their phase transitions (Fig. 1b). The practical consequence of this is that one can never have an OCM that gives a high conversion for both Reaction 2 and Reaction 3 at the same time (Fig. 1c and 1d). The chemical-looping reactor's operation is also compromised thermodynamically because the driving force for oxygen exchange between gas and solid can never be vanishingly small. This is because the oxygen resides in the solid at a fixed oxygen chemical potential, whereas in the gas phase, there is a variable oxygen chemical potential as the gas composition must, for any reasonable conversion, change significantly between reactor inlet and outlet. In fact by some measures such a reactor can perform no better than a conventional 'mixed' reactor (Supplementary Video 1 and Supplementary Information Section 2).

An alternative way of viewing the process is that the OCM is required to transfer chemical information between the H_2O-feed half cycle and CO-feed half cycle for the reactor to operate. A conventional metal-metal oxide system involving a single phase transition (between metal and metal oxide) stores no information about the oxygen chemical potential of the gases to which it has been exposed other than they were sufficiently reducing or oxidising to cause the phase transition. So a single OCM does not have the chemical memory to transfer sufficient information (i.e., the full oxidising and reducing potential of feed gases) for the reactor to achieve high conversions in both half cycles. In theory, it would be possible to transfer more information between half cycles by using axially-separated OCMs with differing oxygen chemical potentials associated with their phase transitions and moving to a

reverse flow design (oxidising and reducing feeds are fed to opposite end of the reactor). The OCMs would need to be spatially arranged such that the most easily oxidised is at the end of the bed which is exposed to the oxidising feed and the most easily reduced at the reducing feed end. We show in the Supplementary Information that, for the WGS reaction at 820°C, if n phase transitions are available using a series of n conventional OCM materials, a maximum conversion of $n/(n+1)$ can be achieved (Supplementary Information Section 2). Unfortunately, this approach, whilst an improvement, would require large numbers of different OCMs to achieve high conversions and would be inflexible if the redox ability of feeds and/or products were changed. If two phase transitions were available within a single material a further benefit can be gained[20] but the system would still lack the flexibility to respond to changing inlet redox abilities (full discussion in Supplementary Information Section 2).

Here we demonstrate that a 'chemical memory reactor' can be built using a single OCM capable of transferring the necessary information for thermodynamically reversible operation between the two half cycles. The OCM can only perform this function in the absence of mixing in the solid phase in order to allow spatially-resolved information to be stored, transferred between half cycles and subsequently read. The oxidising end of the bed must remember the oxygen chemical potential of the most oxidising gas it experiences and the reducing end must remember the oxygen chemical potential of the most reducing gas it experiences throughout the cycles. We therefore need an oxygen carrier that can support the full range of oxygen chemical potentials required (Figure 1e and 1f). This leads us to select an oxide of variable oxygen non-stoichiometry as OCM[21,22], such OCMs having been used previously in chemical looping for kinetic or stability benefits[23,24]. In these materials we know that the oxygen content will be a continuous function of oxygen chemical potential (furthermore we employ oxidising and reducing streams that can exhibit defined oxygen

chemical potentials, here achieved by the presence of two distinct redox couples, H_2/H_2O and CO_2/CO). To summarise, in order to transfer the chemical information required between half cycles, we must simultaneously use reverse flow (so that one end of the bed is always oxidised and the other always reduced), we must use a solid that can support the full range of oxygen chemical potentials required (so that its state can reflect that of the reactant streams) and we must use a solid phase held within a fixed bed (so that solid phase mixing does not result in loss of chemical information).

Our 'chemical memory reactor' then consists of a bed of a non-stoichiometric oxide OCM operated in reverse gas flow (Fig. 1e and 1f) which permits an extensive exchange of chemical information through the OCM between each half cycle. Repeated application of the oxidising feed to the oxidising end of the bed and the reducing feed to the reducing end of the bed causes an oxidation state profile to develop along the length of the bed (Fig. 1g and 1h and Supplementary Video 1). Provided each half cycle is short enough that we do not destroy this oxidation state profile ('memory'), the bed will 'remember' the oxygen chemical potentials associated with its feed streams. The gradual oxidation state profile also leads to small thermodynamic driving forces for the reactions occurring at each point along the reactor's length and tit therefore approaches reversible operation. Whilst recognizing the constraint that the reducing product stream can be no more reducing than the reducing feed and the oxidising product stream no more oxidising than the oxidising feed, we may achieve arbitrarily high overall conversion of the individual Reactions 2 and 3 and hence the overall Reaction 1.

Results

To prove both the concept and the mechanism, an unmixed water-gas shift reaction was performed in such a reverse-flow memory reactor with a non-stoichiometric LSF ($La_{0.6}Sr_{0.4}FeO_{3-\delta}$) perovskite oxygen-carrier material (Supplementary Information Section 1). The nominal temperature of operation (820°C) was chosen such that the equilibrium constant for the conventional mixed water-gas shift reaction (Reaction 1), K, is unity (the measured temperature in the reactor ranges from 790°C to 820°C causing the equilibrium constant to vary between 1.12 and 1.01). $La_{0.6}Sr_{0.4}FeO_{3-\delta}$ was judged to be appropriate for use at this temperature as it is known to be both oxygen non-stoichiometric and stable over a very large range of oxygen chemical potentials, and remains single phase throughout the temperature and oxygen partial pressure range of our experiments. At the temperature of operation, oxygen capacity comes from reduction of Fe(III) to Fe(II) accompanied by oxygen vacancy formation. Oxygen is able to rapidly enter and leave the OCM structure as a result of both high oxygen-ion and electron conductivity.

The reactor was housed in a custom-made furnace and operated at the high-resolution x-ray powder diffraction beam line (ID22) of the European Synchrotron Radiation Facility (ESRF). As an indicator that equilibrium has been overcome, we evaluate for each cycle a variable, K^* (Supplementary Information Section 2), which measures the reactor performance and is maximised for simultaneously high conversions to both H_2 and CO_2,

$$K^* = \frac{\bar{y}_{H_2}\bar{y}_{CO_2}}{\bar{y}_{H_2O}\bar{y}_{CO}} \qquad \text{Equation 1}$$

where $\bar{y}_i$ is a time-averaged mole fraction at the reactor outlet. For a conventional mixed-reactant reactor, K^* would never be able to exceed the water-gas-shift equilibrium constant, K, of unity. Practically this means that conversions to H_2 and CO_2 would not be able to

exceed 50% for a stoichiometric feed. Similarly, the $n/(n+1)$ conversion limitation discussed above means that K^* can never exceed unity for an oxygen-carrier material with a single phase-transition such as that in Fig. 1c and 1d. Our non-stoichiometric oxide, however, behaves as if it supplies a very large number of phase transitions and thus there is no upper limit to the value of K^*. Experimentally, we observe K^* values much greater than unity when we operate our reactor as shown in Fig. 2a. As the bed used was prepared in an oxidised state, initial high conversions of CO to CO_2 are achieved with lower conversions of H_2O to H_2 (Region A of Fig. 2a and Supplementary Fig. 7). After cycling, a profile of oxidation state of the material becomes established and each cycle becomes repeatable with conversions of H_2O and CO equal within uncertainty (as the amount of oxidation in a H_2O-feed half cycle must equal the reduction in a CO-feed half cycle), and both in excess of 75%; K^* is observed to have a value of approximately 14 (Region B of Fig. 2a, Fig. 2b and Supplementary Fig. 7). It is quite clear that equilibrium limitations ($K^* = 1$) have been overcome. Furthermore, the behaviour of the reactor was modelled by assuming plug-flow in the gas phase and gas-solid equilibrium with no adjustable parameters (Supplementary Information Section 7). Fig. 2e shows the outlet mole fractions versus time from the model. Good agreement is seen with Fig. 2b and similar conversions and value of K^* are predicted. By simple valve switching our reactor produces the pure, separated H_2 and CO_2 products of Reaction 1 from different ends of the bed.

Spatially- and temporally-resolved powder x-ray diffraction was used to investigate the state of the LSF oxygen-carrier material during reactor operation (there was no evidence for the formation of any additional phases during operation). Shifts in 2θ peak positions (Fig. 3a, Supplementary Fig. 3 and more discussion in Supplementary Information Section 4) were used to determine changes in lattice parameter which, with calculated chemical and thermal expansion coefficients and a defect chemistry model (Supplementary Information Section 1),

were used to calculate the oxygen content of the material as a function of position in the bed immediately after oxidation and reduction half cycles (Fig. 3b). It is evident that a profile in the oxidation state of the non-stoichiometric material has developed as predicted. Furthermore, although the degree of oxidation of the OCM increases after bed oxidation at every location investigated in the bed compared to immediately after bed reduction, it is clear that the bed retains an oxidation state profile throughout.

To test the concept of chemical memory further we predict that we can improve the memory of the bed and improve conversions by shortening the half-cycle durations (less oxygen is removed and added in each cycle). Thus we see in Fig. 2c, that when the half-cycle duration is reduced from 60 seconds to 48 seconds both conversions increase from in excess of 75% to in excess of 80%, and K^* doubles from 14 to 28. When the duration increases, Fig. 2d, we expect a loss of memory and we see that a 120-second duration results in a decrease of conversions to barely more than 50%; K^* decreases to 1.4. This dependence of K^* on half-cycle duration is also confirmed by use of the thermodynamic model of the reactor (Fig. 2e, Fig. 2f, Fig. 2g). The model predicts values of K^* in Regions B, C and D of 13, 41 and 1.35 compared to the experimentally obtained values of 14, 28 and 1.4. Thus it appears that the reactor does not suffer from significant kinetic limitations. Furthermore, we may use a reactor bed with a fully developed oxidation state profile for the reverse water-gas shift reaction (Supplementary Fig. 9). By feeding H_2 to the reduced end of the bed and CO_2 to the oxidised end we instantly achieve conversions in excess of equilibrium limitations. Such facile switching between forward and reverse reactions is unique to a reversibly-operated chemical memory reactor.

Discussion

The hydrogen produced by the reactor is free of carbon monoxide as no carbon is carried over from the reduction cycle to the hydrogen production cycle. This addresses a key challenge in hydrogen production. Furthermore, because of a lack of equilibrium limitations, the exothermic reaction can be performed at high temperature (taking a high temperature feed from a reforming or gasification process) and thus capitalise on the high kinetic rates available, even in the absence of a shift catalyst. So, whereas conventional hydrogen production requires two reactors (a high and a low temperature shift reactor) to drop carbon monoxide mole fractions to reasonable levels and then a separation step to remove carbon dioxide from the hydrogen, our reactor accomplishes all of these steps in one unit and has kinetics that are more favourable than a conventional process. This, if applied practically, could lead to significantly reduced hydrogen-production process footprints and costs. We must also note that the OCM is stable over a larger number of cycles. 300 cycles were performed with no measurable deterioration in K^* (Supplementary Fig. 7) or change in OCM morphology (Supplementary Fig. 8). The origin of the OCM stability presumably results from the ability of the OCM to donate and receive oxygen without a phase change.

It may be possible to implement more complex reaction schemes involving the introduction of methane (or natural gas) as the reducing feed. Internal reforming of the methane with lattice oxygen from the OCM would result in syngas formation. It would be possible to operate such a reactor in a number of modes optimised for e.g. combined syngas and hydrogen production or hydrogen production alone. Depending on the application area more than two feeds could be desirable with the use of, e.g., an air feed to ensure an overall autothermal process if reforming a hydrocarbon feed. This raises the possibility of using single reactors, albeit dynamically operated, for the conversion of natural gas to hydrogen.

It must be noted that the ‘memory reactor’ concept developed here does not only apply to oxygen exchange reactions. Materials with non-stoichiometry in, e.g., hydrogen also

exist. It may be possible to apply such materials to reversibly couple hydrogenation and dehydrogenation reactions. This application could be crucial if chemical hydrogen storage becomes more important as one would be able to regenerate hydrogen at its supply pressure without significant energy input.

Methods

Material synthesis

$La_{0.6}Sr_{0.4}FeO_3$was synthesised via the sol-gel method using stoichiometric ratios of $Fe(NO_3)_3(H_2O)_9$ (Sigma Aldrich 216828), $La(NO_3)_3(H_2O)_6$ (Sigma Aldrich 61520), and $Sr(NO_3)_2$ (Sigma Aldrich 243426) mixed with citric acid (Sigma Aldrich 791725) and ethylene glycol (Sigma Aldrich 324558) in molar ratios to the total cations present of 1:1 and 1.2:1 respectively. The total cation quantity was chosen to make 100 g of $La_{0.6}Sr_{0.4}FeO_3$. 450 mL of deionised H_2O was added and the solution was stirred, decanted into a 10 L beaker and dried at 60°C for 48 hours. The resulting orange cake was lightly crushed and placed in a covered 700 mL alumina high form crucible and heated to 1050°C at 1°C min^{-1} and held for 18 hours. The resulting powder was then sieved to select particle sizes between 80 and 160 μm.

Flow system and reference experiments

The flow system (Supplementary Fig. 2) employed 4-way cross-over valves to switch the gas composition being fed to the fixed-bed reactor, switch direction of feed to the reactor and to maintain continuous flow through the reactor and the gas analysis equipment. One complete redox cycle contained six phases, two phases of reactive gas feed of CO or H_2O and four

phases with an inert (argon) feed. The directional change of the feed to the reactor was always performed during an inert feed.

The system was operated with a furnace set point of 820°C in a vertical orientation for the *operando* x-ray diffraction studies on ID22 at ESRF and in a horizontal orientation for a long-term stability experiment (Supplementary Fig. 7), the reverse WGS experiment (Supplementary Fig. 9) and two further reference experiments involving a conventional mixed-reactant WGS experiment and an empty reactor with unmixed reactants (Supplementary Fig. 10). All total flows were set (unless otherwise stated) to 3.4×10^{-5} mol s^{-1} (50 ml min^{-1} at NTP).

Operando XRD setup

The *operando* XRD reactor bed was held in a vertical furnace at a nominal 820°C and consisted of LSF641 powder, 1.43 g (6.43×10^{-3} mol), packed into a quartz tube with an internal diameter of 4 mm with 2 mm wall thickness to form a fixed-bed reactor that was 114.5 mm long. Local temperature was recorded with a K-type thermocouple placed in contact with the reactor tube which was allowed to equilibrate over 10 minutes. The local temperature was found to be 790°C at the bottom of the reactor bed, 810°C in the middle and 820°C at the top. This leads to a thermally-induced variation of oxygen content in the absence of reaction which is accounted for in our analysis.

Operando X-ray powder diffraction was conducted at the high-resolution powder diffraction beamline ID22 at ESRF (MA2914) using the multi-analyser stage[25]. The energy used was 38 keV. The multi-analyser stage is composed of nine Si 111 analyser crystals preceding nine scintillator detectors, the detector channels being 2 degrees apart. The 2θ arm was scanned from 9 to 11.2 degrees (2θ) at a speed of 4 degrees min^{-1}. This setup yielded a

total effective scan range of 1 to 19.2 degrees, binned to 0.002 degree resolution, with 0.2 degree overlap between each detector. The effective scan time was 36 seconds when initialisation of the positioner at the beginning of each scan was taken into account.

Data availability statement

Data supporting this publication is openly available under an "Open Data Commons Open Database License". The data with additional metadata are available at http://dx.doi.org/10.17634/080913-1

References

1. Dincer, I., Cengel Y. A. Energy, entropy and exergy concepts and their roles in thermal engineering. *Entropy* **3**(3), 116-149 (2001).
2. Dunbar W. R., Lior N. Sources of combustion irreversibility. *Combust. Sci. Technol.* **103**, 41-61 (1994).
3. Dudukovic M. P. Frontiers in Reaction Engineering. *Science* **325**, 698-701 (2009).
4. Thursfield A., Murugan A., Franca R., Metcalfe I. S. Chemical looping and oxygen permeable ceramic membranes for hydrogen production-a review. *Energy & Environ. Sci.* **5**, 7421-7459 (2012).
5. Adanez J., Abad A., Garcia-Labiano F., Gayan P., de Diego L. F. Progress in chemical-looping combustion and reforming technologies. *Prog. Energy Combust. Sci.* **38**, 215-282 (2012).
6. Fan L.S., *Chemical looping systems for fossil energy conversions*. (Wiley-AIChE, Hoboken, NJ, 2010), pp. 241-249.
7. Lyngfelt A., Leckner B., Mattisson T. A fluidised-bed combustion process with inherent CO_2 separation; application of chemical-looping combustion. *Chem. Eng. Sci.* **56**(10), 3101-3113 (2001).
8. Richter H. J., Knoche K. F. Reversibility of Combustion Processes. *Acs Sym Ser* **235**, 71-85 (1983).
9. Anhedena M., Svedberga G. Exergy analysis of chemical-looping combustion systems. *Energ. Convers. Manag.* **39**, 1967-1980 (1998).
10. U.S. Department of Energy Hydrogen and Fuel Cell Technical Advisory Committee, "Report of the Hydrogen Production Expert Panel" (2013; www.hydrogen.energy.gov/pdfs/hpep_report_2013.pdf).
11. Lu G. Q., da Costa J. C. D., Duke M., Giessler S., Socolow R., Williams R. H., Kreutz T. Inorganic membranes for hydrogen production and purification: A critical review and perspective. *J. Colloid Interface Sci.* **314**, 589-603 (2007).
12. Giessler S., Jordan L., da Costa J. C. D., Lu G. Q. Performance of hydrophobic and hydrophilic silica membrane reactors for the water gas shift reaction. *Sep. Purif. Technol.* **32**, 255-264 (2003).

13. Basile A., Criscuoli A., Santella F., Drioli E. Membrane reactor for water gas shift reaction. *Gas Sep. Purif.* **10**, 243-254 (1996).

14. Noor T., Gil M. V., Chen D. Production of fuel-cell grade hydrogen by sorption enhanced water gas shift reaction using Pd/Ni-Co catalysts. *Appl. Catal., B* **150**, 585-595 (2014).

15. Jang H. M., Kang W. R., Lee K. B. Sorption-enhanced water gas shift reaction using multi-section column for high-purity hydrogen production. *Int. J. Hydrogen Energy* **38**, 6065-6071 (2013).

16. Jang H. M., Lee K. B., Caram H. S., Sircar S. High-purity hydrogen production through sorption enhanced water gas shift reaction using K_2CO_3-promoted hydrotalcite. *Chem. Eng. Sci.* **73**, 431-438 (2012).

17. Harrison D. P. Sorption-enhanced hydrogen production: A review. *Ind. Eng. Chem. Res.* **47**, 6486-6501 (2008).

18. Ortiz A. L., Harrison D. P. Hydrogen production using sorption-enhanced reaction. *Ind. Eng. Chem. Res.* **40**, 5102-5109 (2001).

19. Balasubramanian B., Ortiz A. L., Kaytakoglu S., Harrison D. P. Hydrogen from methane in a single-step process. *Chem. Eng. Sci.* **54**, 3543-3552 (1999).

20. Kathe M. V., Empfield A., Na J., Blair E., Fan L-S. Hydrogen production from natural gas using an iron-based chemical looping technology: Thermodynamic simulations and process system analysis. *Appl. Energy* **165**, 183-201 (2016).

21. Mizusaki J., Yoshihiro M., Yamauchi S., Fueki K. Nonstoichiometry and defect structure of the perovskite-type oxides $La_{1-x}Sr_xFeO_{3-\delta}$. *J. Solid State Chem.* **58**, 257-266 (1985).

22. Sogaard M., Hendriksen P. V., Mogensen M. Oxygen nonstoichiometry and transport properties of strontium substituted lanthanum ferrite. *J. Solid State Chem.* **180**, 1489-1503 (2007).

23. Rydén M., Lyngfelt A., Mattisson T., Chen D., Holmen A., Bjørgum E. Novel oxygen-carrier materials for chemical-looping combustion and chemical-looping reforming; $La_xSr_{1-x}Fe_yCo_{1-y}O_{3-\delta}$ perovskites and mixed-metal oxides of NiO, Fe_2O_3 and Mn_3O_4. *Int. J. Hydrog. Energy* **2**, 21-36 (2008).

24. Murugan A., Thursfield A., Metcalfe I. S. A chemical looping process for hydrogen production using iron-containing perovskites. *Energy Environ. Sci.* **4**, 4639-4649 (2011).

25. Hodeau J-L., P. Bordet, Anne M., Prat A., Fitch A. N., Dooryhee E., Vaughan G., Freund A. K. Nine-crystal multi-analyser stage for high resolution powder diffraction between 6 and 40 keV. *SPIE Proceedings* **3348**, 353-361 (1998).

Acknowledgments

CT, CdL thank EPSRC for funding via a doctoral training award. The research leading to these results has received funding from the European Research Council under the European Union's Seventh Framework Programme (FP/2007-2013) / ERC Grant Agreement Number 320725 and from the EPSRC via grants EP/G012865/1, EP/J016454/1 and EP/K029649/1, EP/P007767/1, EP/P024807/1. We thank Andy Fitch, Carlotta Giacobbe, Mauro Coduri and Olivier Grimaldi at ESRF for help with XRD and Trevor Ingham, IGI Systems Ltd., for constructing the custom flow system and furnace. We thank Alan Coelho for developments in Topas to enable analysis of the multiple x-ray data sets produced. We thank Dr Brad Ladewig with help in producing the video.

Author contributions

ISM conceived the overall idea, secured funding, and managed the work. ISM, JSOE wrote the main text. ISM, BR, WH, CdL, JSOE were responsible for the data analysis, modelling and interpretation. BR, CD, CdL, CD, FGG, CM, EIP, CRT, performed the experiments.

Competing interests

The authors declare no competing interests.

Additional information

Supplementary Information is linked to the online version of the paper at www.nature.com/nchem/.

Correspondence and requests for materials should be addressed to ian.metcalfe@newcastle.ac.uk.

List of figure captions

Fig. 1. Thermodynamic reversibility in a water-gas shift reactor. Colour coding of oxygen chemical potentials in the gas phase and oxygen content in the solid phase (red to blue for oxidising to reducing) is used to show that within conventional mixed gas reactors and metal-metal oxide chemical looping reactors the reactants cannot be fully converted. (**a**) Conventional WGS reactor producing a mixture of reactants and products. (**b**) Equilibrium relationship for a metal-metal oxide showing solid-phase oxygen content versus oxygen chemical potential of the gas phase. Note that only orange and light blue potentials are required to show where the phase transition lies. (**c**) The use of such a metal-metal oxide OCM for H_2 production in a chemical looping cycle where water is fed over the metal. The phase transition is not sufficiently reducing to produce a high mole fraction of H_2. (**d**) Reduction of the metal oxide (CO is fed from the opposite end of the bed to H_2O) cannot produce a high mole fraction of CO_2. (**e**) The mode of operation of our memory reactor. The reactor contains a non-stoichiometric oxygen carrier (e.g. a perovskite, $ABO_{3-\delta}$) and operates under reverse flow with feeds of 5% CO (during the reduction step) and 5% H_2O (during the oxidation step). The reactive stages are preceded and followed by a flow of argon. (**f**) Equilibrium relationship for a non-stoichiometric oxide showing solid-phase oxygen content versus gas phase oxygen chemical potential. Note that oxygen capacity is available over the entire range of oxygen chemical potentials. (**g** and **h**) A non-stoichiometric oxide develops a profile of oxidation states along the bed allowing the production of pure products if cycle durations do not remove the profile from the bed. (**g**) A H_2O feed is converted almost entirely to H_2 as the H_2 exits over the reduced end of the bed before (**h**) switching the direction of flow and converting CO almost entirely to CO_2 as the CO_2 exits over the oxidised end of the bed. More explanation of the reactor concept can be found elsewhere (Supplementary Video 1).

418

419 **Fig. 2. Conversion, reactor performance measure (*K**) and outlet mole fractions (real**
420 **and modelled) versus cycle number show that equilibrium limitations have been**
421 **overcome.** (**a**) Time-averaged conversions of CO ($\bar{x}_{CO}$, squares) and H_2O ($\bar{x}_{H_2O}$, triangles)
422 on the left axis and reactor performance measure, *K**, on the right axis, as a function of cycle
423 number for a reverse-flow memory reactor containing non-stoichiometric $La_{0.6}Sr_{0.4}FeO_{3-\delta}$.
424 Region A (evolution of the oxidation state profile) (Cycles 1-15) with 60-second feeds of CO
425 and H_2O, Region B (Cycles 16-30) with 60-second feeds, Region C (Cycles 31-45) with 48-
426 second feeds, and Region D (Cycles 46-60) with 120-second feeds. The dashed lines are
427 equivalence lines between an overall conversion and the corresponding measure of reactor
428 performance. Note, that the *K** for Cycle 46 is 0.7 and is off-scale. The small difference
429 between the conversions of CO and H_2O are due to small differences in the flowrates
430 between oxidising and reducing half cycles; the oxygen balance closes to within 97%. (**b**),
431 (**c**) and (**d**) Measured effluent gas mole fractions versus time for representative cycles. (**e**),
432 (**f**) and (**g**) Corresponding modelled effluent gas mole fractions versus time.

433

434 **Fig. 3. Representative shifts in 2θ peak positions and local oxygen content of the**
435 **$La_{0.6}Sr_{0.4}FeO_{3-\delta}$ versus reactor position showing changes in lattice parameter and**
436 **oxygen content are a function of axial position.** (**a**) *Operando* XRD scans, arbitrary
437 intensity, from the H_2O-feed end of the reactor bed after the CO feed of Cycle 22 (red
438 triangles) and the H_2O feed of Cycle 23 (blue squares) showing the lower 2θ peak positions
439 and thus larger cubic lattice parameter after CO feed compared to H_2O feed. (**b**) Local
440 oxygen content of the non-stoichiometric solid ($La_{0.6}Sr_{0.4}FeO_{3-\delta}$), 3-δ, relative to the local
441 oxygen content of the reactor bed in the absence of chemical reaction, 3-δ*, versus reactor
442 position, for Region B in Fig. 2, immediately after oxidation (red triangles) and reduction
443 (blue squares). The CO-feed end of the reactor remained the most reduced location (lowest
444 oxygen content) and the H_2O-feed end of the reactor the most oxidised (highest oxygen
445 content). There is a profile in oxygen content which, although shifted, from oxidation to
446 reduction, retains a memory of the gas feeds.

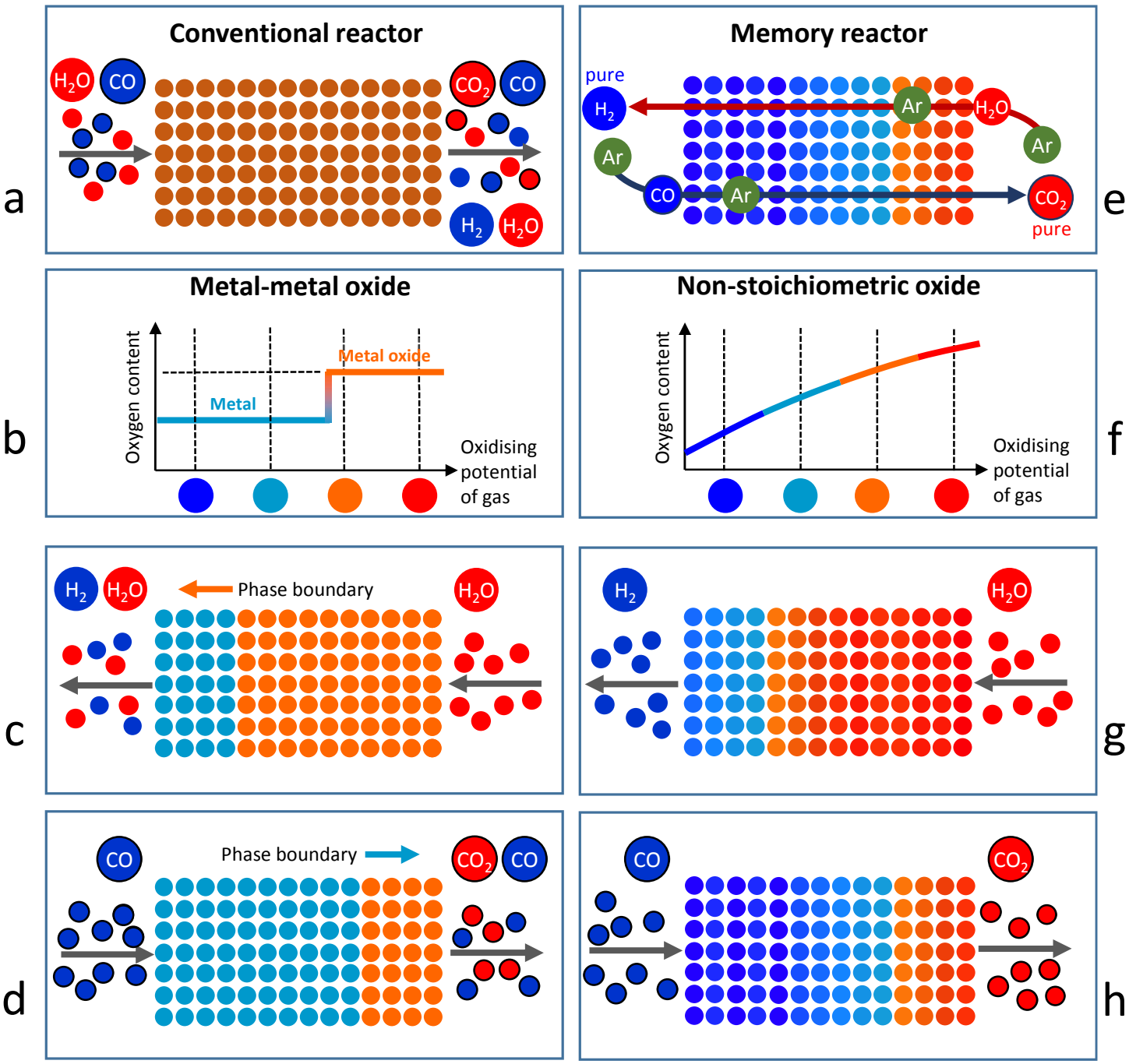
a
Conventional reactor
H_2O
CO
CO_2
CO
H_2
H_2O
e
Memory reactor
pure
H_2
Ar
H_2O
Ar
Ar
CO
Ar
CO_2
pure
b
Metal-metal oxide
Oxygen content
Metal oxide
Metal
Oxidising potential of gas
f
Non-stoichiometric oxide
Oxygen content
Oxidising potential of gas
c
H_2
H_2O
Phase boundary
H_2O
g
H_2
H_2O
d
CO
Phase boundary
CO_2
CO
h
CO
CO_2

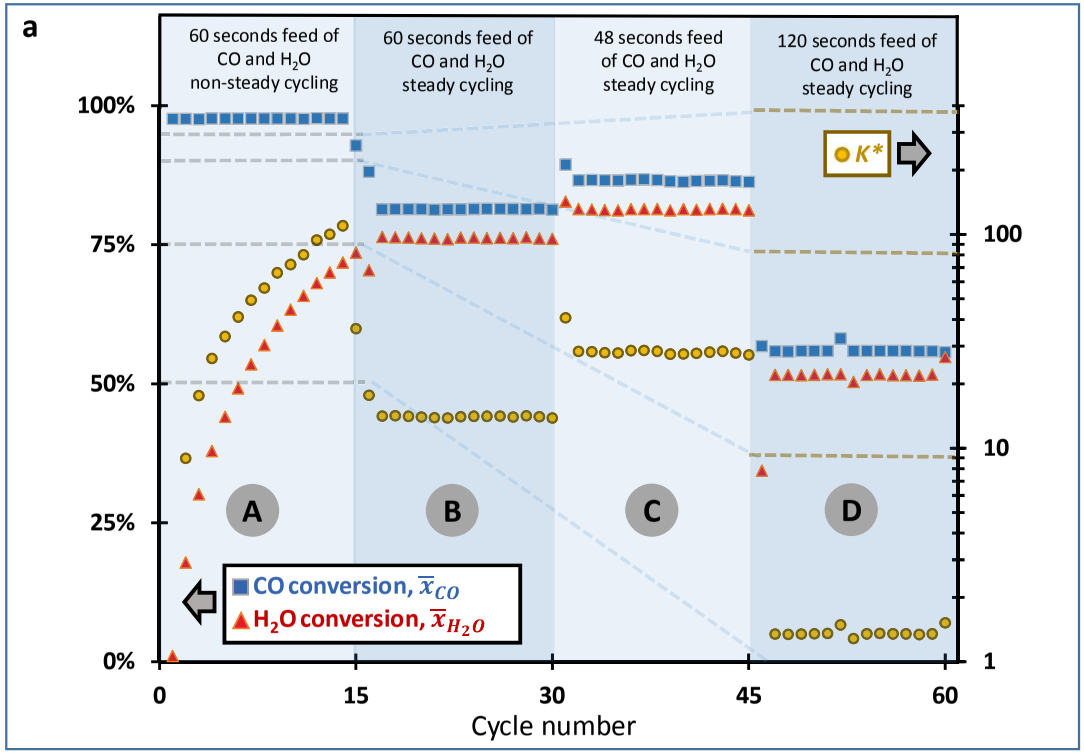
a
60 seconds feed of CO and H2O non-steady cycling
60 seconds feed of CO and H2O steady cycling
48 seconds feed of CO and H2O steady cycling
120 seconds feed of CO and H2O steady cycling
K*
100%
75%
50%
25%
0%
100
10
1
A
B
C
D
CO conversion, $\overline{x}_{CO}$
H2O conversion, $\overline{x}_{H_2O}$
0
15
30
45
60
Cycle number

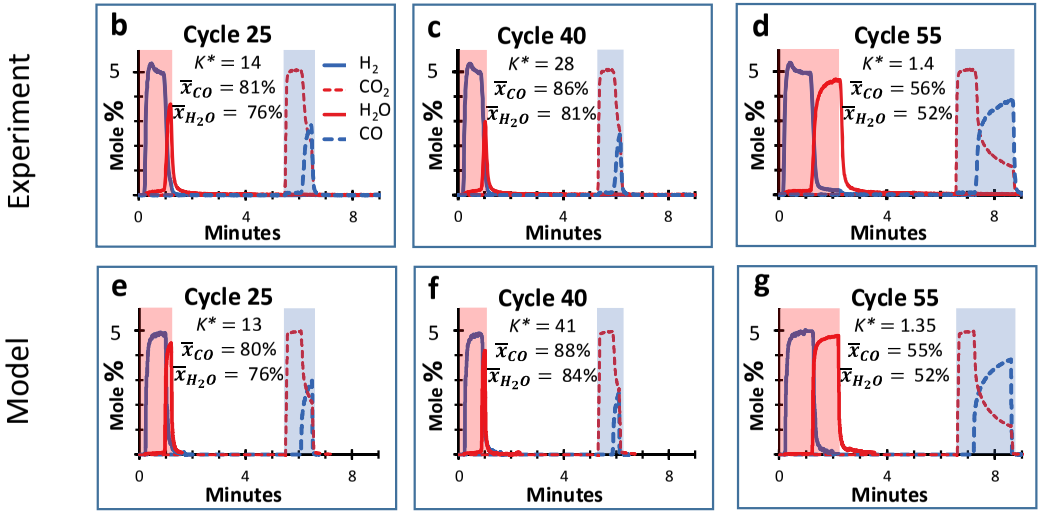
Experiment
Model
b
Cycle 25
K* = 14
$\overline{x}_{CO}$ = 81%
$\overline{x}_{H_2O}$ = 76%
c
Cycle 40
K* = 28
$\overline{x}_{CO}$ = 86%
$\overline{x}_{H_2O}$ = 81%
d
Cycle 55
K* = 1.4
$\overline{x}_{CO}$ = 56%
$\overline{x}_{H_2O}$ = 52%
e
Cycle 25
K* = 13
$\overline{x}_{CO}$ = 80%
$\overline{x}_{H_2O}$ = 76%
f
Cycle 40
K* = 41
$\overline{x}_{CO}$ = 88%
$\overline{x}_{H_2O}$ = 84%
g
Cycle 55
K* = 1.35
$\overline{x}_{CO}$ = 55%
$\overline{x}_{H_2O}$ = 52%
H2
CO2
H2O
CO
Mole %
Minutes
0
4
8
5

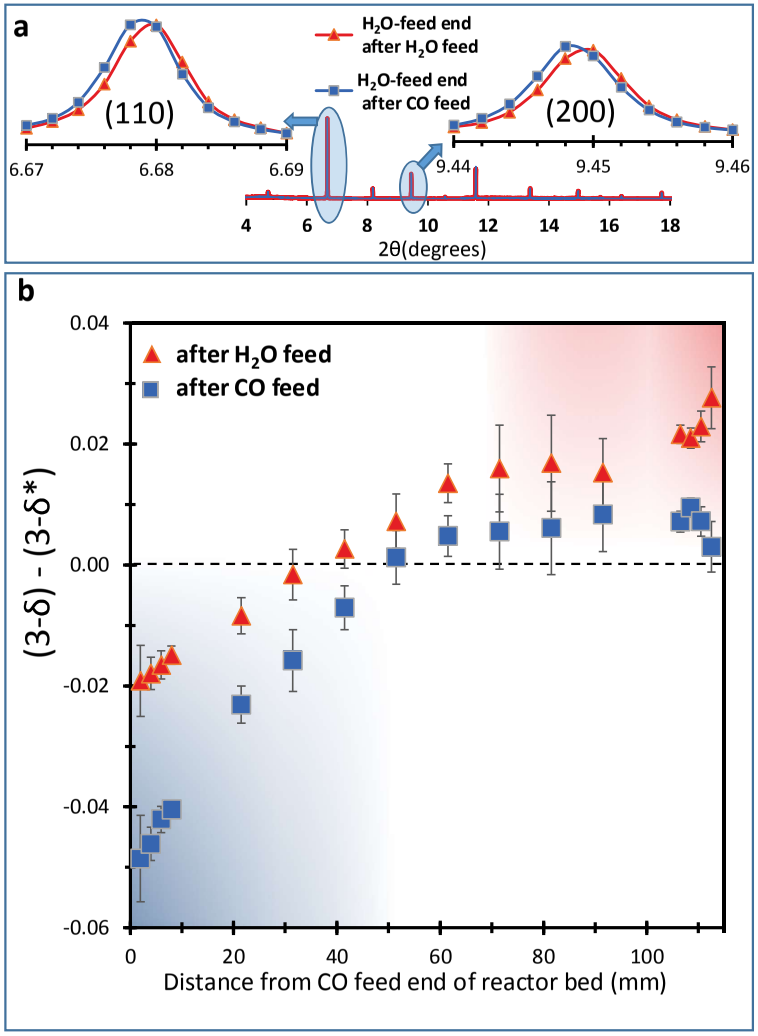
a
H2O-feed end after H2O feed
H2O-feed end after CO feed
(110)
(200)
6.67
6.68
6.69
9.44
9.45
9.46
4
6
8
10
12
14
16
18
2θ(degrees)
b
after H2O feed
after CO feed
0.04
0.02
0.00
-0.02
-0.04
-0.06
(3-δ) - (3-δ*)
0
20
40
60
80
100
Distance from CO feed end of reactor bed (mm)